

Received March 15, 2020, accepted March 31, 2020, date of publication April 14, 2020, date of current version April 30, 2020.

Digital Object Identifier 10.1109/ACCESS.2020.2987808

Enhanced Power Decoupling Strategy for Virtual Synchronous Generator

MINGXUAN LI¹, (Graduate Student Member, IEEE), YUE WANG¹, (Member, IEEE),
YONGHUI LIU¹, (Graduate Student Member, IEEE), NINGYI XU², SIRUI SHU¹,
AND WANJUN LEI¹, (Member, IEEE)

¹State Key Laboratory of Electrical Insulation and Power Equipment, Xi'an Jiaotong University, Xi'an 710049, China

²State Grid Ningbo Electric Power Supply Company, State Grid Ltd., Ningbo 315000, China

Corresponding author: Yue Wang (davidwangyue@mail.xjtu.edu.cn)

This work was supported in part by the National Natural Science Foundation of China under Grant 51777159, and in part by the China Scholarship Council (CSC) under Grant 201706280149.

ABSTRACT Power coupling caused by high impedance ratio and nonzero power angle is a crucial issue for virtual synchronous generator (VSG), which may result in output power error, slower power response and even invalid operation. To solve this issue, a novel enhanced power decoupling method by using virtual steady-state synchronous impedance (VSSI) and current dynamic decoupling compensation (CDDC) is proposed. VSSI with the unique characteristic that the value of virtual reactance maintains constant in all frequencies, can solve the power coupling caused by impedance ratio. CDDC can solve the power coupling caused by nonzero power angle in the fastest way by the designed compensation in inner current loop. The reshaped output impedance characteristics are also analyzed in detail. Then, by state-space modelling and analysis, it is proved that, compared to the traditional methods, the proposed method can improve the dynamic performance and enhance the system stability further. Finally, the results of comparative experiments demonstrate that the proposed method can solve the power coupling problem more effectively and improve the dynamic and steady-state responses of active power and reactive power.

INDEX TERMS Virtual synchronous generator (VSG), power decoupling, virtual impedance, oscillation suppression.


I. INTRODUCTION

The development of renewable energy sources (RESs), such as photovoltaics and wind power generation, plays an important role in responding to the energy crisis and environmental problems [1]. However, the RESs mostly interface with the power grid by grid-connected converters, which lack inertia and damping and have weak support capability of frequency and voltage [2]–[4]. As a consequence, a huge challenge has been posed, that is how to maintain the stable operation of the power system with high penetration of grid-connected converters [5]. To cope with this challenge, the concept of virtual synchronous generator (VSG) control [6]–[11], also called virtual synchronous machine (VISMA) [12], [13], or synchronverter [14], has been proposed. VSG firstly emulates the function of primary frequency and voltage regulation of synchronous generator (SG)

by using droop control. Furthermore, VSG mimics the swing equation of SG to increase the inertia of grid-connected converter and improve the transient response characteristics. VSG has become a promising approach for interfacing RES with power systems due to its excellent features.

The foundation of normal operation of VSG is the decoupling characteristics of power flow through transmission line, that is, for the circumstances of a small power angle and pure inductive impedance between two voltage sources, the active power depends predominantly on voltage frequency, whereas reactive power depends predominantly on voltage amplitude [15]. However, the two fundamental preconditions, i.e. small power angle and pure inductive impedance, are not always satisfied. As a result, the dynamic performance and stability of VSGs are deteriorated.

VSG is often linked to low-voltage lines/networks, where the impedance ratio R/X is high. Consequently, the aforesaid power decoupling precondition cannot be satisfied. To solve this problem, four groups of power decoupling

The associate editor coordinating the review of this manuscript and approving it for publication was Mohsin Jamil .

methods, mainly including virtual impedance method [15]–[18], virtual power method [19]–[21], virtual frequency and voltage method [22] and power feedforward compensation method [23]–[26], are proposed. The idea of virtual impedance method is to reshape the output impedance of VSG to become mainly inductive by implementing a virtual impedance loop. The virtual power method and virtual frequency and voltage method, are to rotate the vectors of active power and reactive power by an impedance angle, or to rotate the vectors of frequency and voltage amplitude, so as to obtain the mutually independent relationship. The power feedforward compensation method is to add a pair of cross channels between active power and reactive power control path to counteract the effect of power coupling channel.

The above methods provide effective solutions to address the high impedance ratio issue, but the effect of error due to small power angle assumption is often ignored. However, several phenomena caused by power coupling, e.g. power oscillation, reactive power steady-state error, have been still observed even though the output impedance of VSG is purely inductive [7], [27], [28]. Due to the existence of virtual inertia in VSG, a potential oscillation characteristic will transfer between the active power loop and reactive power loop. Therefore, it causes a dynamic and steady-state performance deterioration in the meanwhile and thereby affects the primary control and power sharing. Besides, the coupling oscillation also damages the VSGs due to their poor overcurrent capacity, and even becomes diverging and makes the system unstable. Hence, the power coupling issue of VSG is much more serious than droop control. To ensure good control performance of VSG, a more accurate decoupling method is necessary to relax the small power angle assumption which may cause the performance degradation and instability problem.

Considering the effect of line impedance ratio and power angle on active power and reactive power control simultaneously, an oscillation suppression method from the perspective of designing optimal damping coefficient is presented in [7]. Dynamic coupling phenomenon is analysed by small-signal modelling and a power oscillation suppression method by adding virtual resistance is proposed in [29]. However, these methods cannot eliminate the coupling between active power and reactive power, and the corresponding issues caused by power coupling, e.g. control error and stability degradation, are not solved. Furthermore, the oscillation suppression capacity of damping coefficient is limited by the trade-off within primary frequency regulation requirement, power oscillation suppression performance and dynamic response time. The virtual resistance can eliminate the oscillation and enhance the stability, but it deteriorates the coupling. The accurate tracking of the voltage in PCC by modifying the excitation voltage regulator is realised to satisfy the requirements of power decoupling in [30], but this method depends on the highly accurate identification of line impedance.

Motivated by this issue, this paper studies an enhanced power decoupling method to improve the performance and

stability of VSG. This method can also be used in other droop-based grid-connected converters. The rest of this paper is organized as follows. In Section II, the basic principle of VSG control is briefly reviewed and the power coupling issue of VSG is analyzed quantitatively by using relative gain array method. In Section III, an accurate power decoupling method is proposed. In Section IV, the dynamic response performance and stability of VSG with the proposed enhanced decoupling strategy are analyzed. The experiment results are shown in Section V. Finally, conclusions are drawn in Section VI.

II. POWER COUPLING ISSUE OF VSG

A. BASIC PRINCIPLE OF VSG CONTROL

The basic structure of VSG system is depicted in Fig. 1. The control strategy is built in d - q reference frame. The power control loop generates the magnitude and frequency of the output voltage reference. The virtual impedance is used to emulate the electric characteristic of the stator in SG. The current control loop adopts PI regulators to realize the accurate tracking property and overcurrent protection function.

Active power loop emulates the function of primary frequency control and rotating inertia of SG, which is expressed mathematically (ignoring the low pass filter) as:

$$P = P_{\text{ref}} - (D + k_p)(\omega - \omega_{\text{ref}}) - J\omega_{\text{ref}} \frac{d\omega}{dt} \quad (1)$$

where P and P_{ref} are the output active power and its reference respectively, ω and ω_{ref} are radian frequency of virtual inner voltage of VSG and the nominal radian frequency, J is the virtual inertia, k_p is the active power droop coefficient, D is the damping coefficient.

The structure of reactive power loop obtains the RMS reference of virtual inner voltage E by Q - E droop control. The reactive power loop ignoring the low pass filter can be expressed as:

$$Q = Q_{\text{ref}} - k_Q(\sqrt{2}E - E_{\text{ref}}) \quad (2)$$

where Q and Q_{ref} are the output reactive power and its reference respectively, E_{ref} and E are the nominal voltage amplitude and the RMS value of virtual inner voltage of VSG, k_Q is the reactive power droop coefficient.

VSG regulates the phase to control the output active power according to (1), and regulates the magnitude of voltage to control the output reactive power according to (2) independently.

B. ANALYSIS OF POWER COUPLING ISSUE

According to the principle of VSG control explained by (1) and (2), in order to ensure the normal operation of VSG, it is necessary that there should exist same decoupling characteristics when power flows through the transmission line. For an AC system with a given transmission line impedance, illustrated in Fig. 2, the active and reactive power flowing

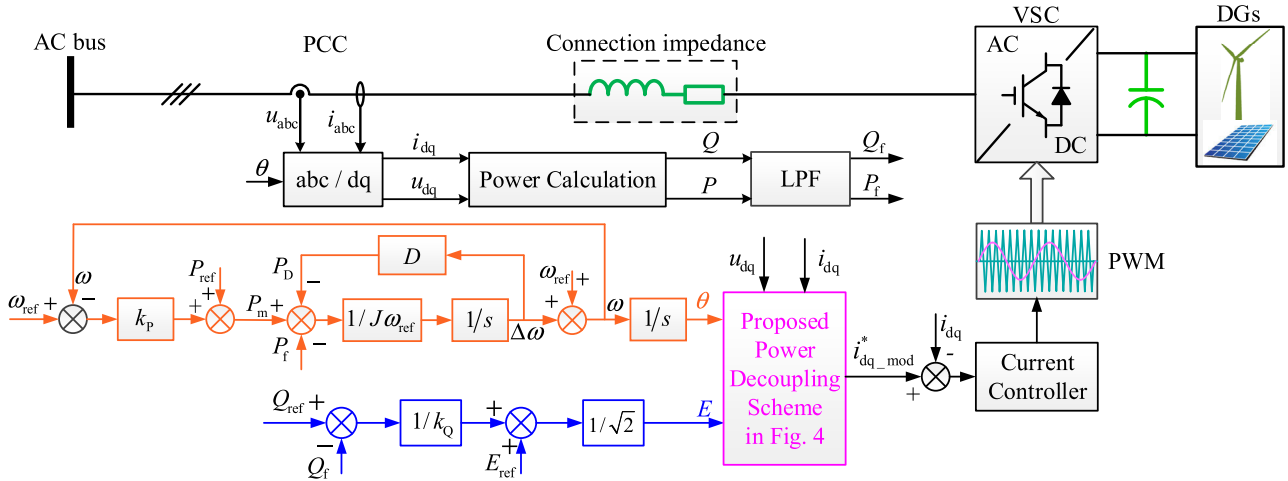


FIGURE 1. The basic control structure of VSG.

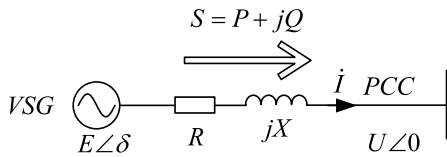


FIGURE 2. Equivalent circuit of a VSG connected to an AC bus.

between two voltage sources can be expressed as

$$\begin{cases} P = \frac{EU}{\sqrt{R^2 + X^2}} \sin\left(\delta + \arctan \frac{R}{X}\right) - \frac{RU^2}{R^2 + X^2} \\ Q = \frac{EU}{\sqrt{R^2 + X^2}} \cos\left(\delta + \arctan \frac{R}{X}\right) - \frac{XU^2}{R^2 + X^2} \end{cases} \quad (3)$$

where R and X are equivalent resistance and reactance between VSG and AC bus respectively, δ is the power angle, E and U are the RMS values of virtual inner voltage and voltage at PCC.

It can be seen that both active power and reactive power are functions of two variables, power angle and voltage magnitude. Linearizing (3) at a steady-state point yields

$$\begin{aligned} \begin{bmatrix} \Delta P \\ \Delta Q \end{bmatrix} &= \begin{bmatrix} \partial P / \partial \delta & \partial P / \partial E \\ \partial Q / \partial \delta & \partial Q / \partial E \end{bmatrix} \Big|_{\substack{\delta = \delta_0 \\ E = E_0}} \begin{bmatrix} \Delta \delta \\ \Delta E \end{bmatrix} \\ &= \frac{U}{\sqrt{R^2 + X^2}} \cdot \begin{bmatrix} E_0 \cos \gamma_c & \sin \gamma_c \\ -E_0 \sin \gamma_c & \cos \gamma_c \end{bmatrix} \begin{bmatrix} \Delta \delta \\ \Delta E \end{bmatrix} \end{aligned} \quad (4)$$

where $\gamma_c = \delta + \arctan(R/X)$, Δ indicates the perturbation of the corresponding variable, the subscript 0 represents the steady-state value.

Expression (4) indicates that when $\gamma_c \neq 0$, the active power and reactive power are coupled with each other rather than mutually independent. Consequently, the active power and reactive power control will be affected by each other and thus the performance and stability will deteriorate.

To quantitatively analyse the coupling degree, relative gain array (RGA) analysis method [31] is used in this paper.

Assuming y_i is the i^{th} controlled variable of a multiple-input-multiple-output (MIMO) system and u_j is the j^{th} manipulated variable, the relative gain of the u_j - y_i channel is defined as the ratio of the u_j - y_i channel gain with other channels open, indicated by p_{ij} , and the u_j - y_i channel gain with other channels closed and other controlled variables constant, indicated by q_{ij} . The mathematical expression can be written as

$$\lambda_{ij} = \frac{p_{ij}}{q_{ij}} = \frac{\partial y_i}{\partial u_j} \Big|_{u_k = \text{const}} \Big/ \frac{\partial y_i}{\partial u_j} \Big|_{y_k = \text{const}} \quad (k \neq j) \quad (5)$$

where ‘‘const’’ represent constant value.

Arranging λ_{ij} in the order marked in subscript can construct the RGA Λ , which describes the coupling relationship and degree of a MIMO system. For the VSG system studied in this paper, the corresponding RGA can be derived as

$$\Lambda = \begin{bmatrix} \lambda_{11} & \lambda_{12} \\ \lambda_{21} & \lambda_{22} \end{bmatrix} = \begin{bmatrix} \cos^2 \gamma_c & \sin^2 \gamma_c \\ \sin^2 \gamma_c & \cos^2 \gamma_c \end{bmatrix} \quad (6)$$

To quantify the coupling level, define relative coupling coefficient K_c as

$$K_c = \lambda_{12} = \sin^2(\delta + \arctan R/X) \quad (7)$$

According to the theory of RGA, a larger K_c indicates a higher coupling level. Only when $K_c \in [0, 0.5]$, the pairing relationship of δ - P and E - Q is satisfied and thereby the effectiveness of the VSG power control loops can be guaranteed. The closer to 0 K_c is, the weaker the coupling is. When $K_c > 0.3$, the coupling becomes quite severe.

Fig. 3(a) shows the curve of K_c vs. δ and R/X . Fig. 3(b) shows the vertical profile of the three-dimensional graph in Fig. 3(a) at different δ . The stability regions of the cases are in the left of the points of $K_c = 1$ which are marked in Fig. 3(b). It can be seen that the stability region gets narrower with the increase of the power angle δ . Taking the curve of $\delta = 0.26$ rad for example, the stability region is located in $R/X < 3.73$. Actually, $K_c = 0.3$ when $R/X =$

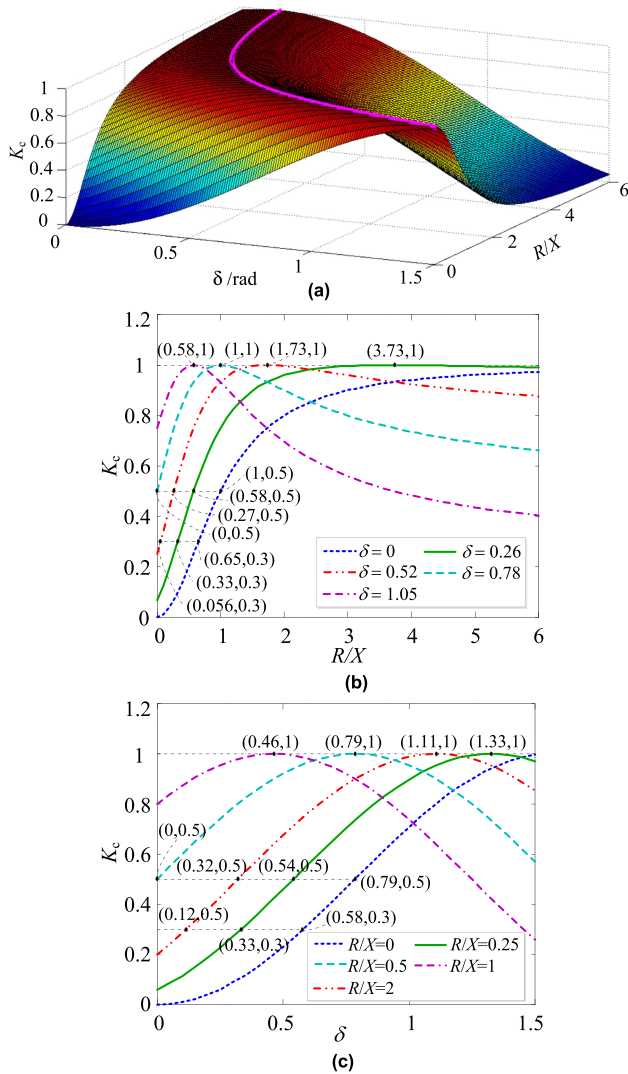


FIGURE 3. The relationship diagrams of K_c vs. δ and R/X (a) K_c vs. δ and R/X , (b) K_c vs. R/X , (c) K_c vs. δ .

0.33, which means that there already exists severe coupling. With the rise of R/X , the level of coupling gets higher. When $R/X > 0.58$, $K_c > 0.5$ and the coupling channel is predominant in controlling the output power.

Fig. 3(c) gives the relationship between K_c and δ for different R/X . Similarly, the stability region gets narrower with the increase of R/X . Taking the curve of $R/X = 0.25$ for example, the stability region is in $\delta < 1.33$ rad. With the rise of δ , the coupling becomes more serious. When δ increases to 0.33 rad, $K_c = 0.3$ and the coupling has become serious. When $\delta > 0.54$ rad, $K_c > 0.5$ and it indicates the coupling channel has a greater influence on the output power than the control channel.

It can be seen from (7) and Fig. 3(c), the coupling level is related not only to the transmission impedance ratio R/X but also to the power angle δ . Only when the transmission is purely inductive and power angle is zero, the active power and

reactive power are decoupled, which meets the prerequisite of VSG control strategy.

III. ENHANCED POWER DECOUPLING METHOD

In order to address the power coupling issue, an enhanced power decoupling method is proposed in this section, which can simultaneously eliminate the power coupling caused by the high impedance ratio and small power angle condition. The droop control can be regarded as a special type of VSG with zero virtual inertia. Therefore, the proposed method can also be used in droop control.

The control strategy mainly contains two parts: virtual steady-state synchronous impedance (VSSI) and current dynamic decoupling compensation (CDDC), where VSSI can eliminate the power coupling caused by the high impedance ratio and CDDC can eliminate the power coupling caused by nonzero power angle δ .

The whole proposed decoupling control block diagram is shown in Fig. 4. The control block of VSSI part is depicted in the green box and control block of CDDC part is depicted in the yellow box and serves as the initial current reference. The d - q reference frame is oriented according to the VSG virtual inner voltage, so that $e_d = E$, $e_q = 0$. Then two pairs of current feedforward references, which are used to eliminate the power coupling caused by the power angle, are added to the initial current reference and then the modified current reference is obtained. After that, the reference goes through PI controller to generate the control signal of converter, where a voltage feedforward is introduced. This method obtains the current reference algebraically with no need of regulator; thus, it has faster regulation performance than cascaded voltage and current controllers.

The principle and implementation of each part are interpreted as follows.

A. VSSI PART

In VSSI, the synchronous admittance matrix is expressed as

$$\mathbf{Y}_{vdq} = \begin{bmatrix} Y_{vdd} & Y_{vdq} \\ Y_{vqd} & Y_{vqq} \end{bmatrix} = \frac{1}{R_v^2 + X_v^2} \begin{bmatrix} R_v & X_v \\ -X_v & R_v \end{bmatrix} \quad (8)$$

where R_v is the virtual resistance, and X_v is the virtual steady-state synchronous reactance that is the product of nominal frequency ω_{ref} and virtual inductance L_v as shown in (9).

$$X_v = \omega_{ref} L_v \quad (9)$$

It should be emphasized that as long as L_v is certain, the value of X_v maintains constant rather than changes with frequency like traditional virtual reactance. The proposed novel design of X_v makes the voltage on it be 90 degrees ahead of the current flowing through it, while its gain amplitude to the current remains constant at all frequencies. That makes VSG with VSSI more stable than VSG with Traditional Virtual Impedance (TVI), which will be demonstrated by root locus in Section IV.

In order to verify the effectiveness of reshaping output impedance in both the resistance and inductance dimensions,

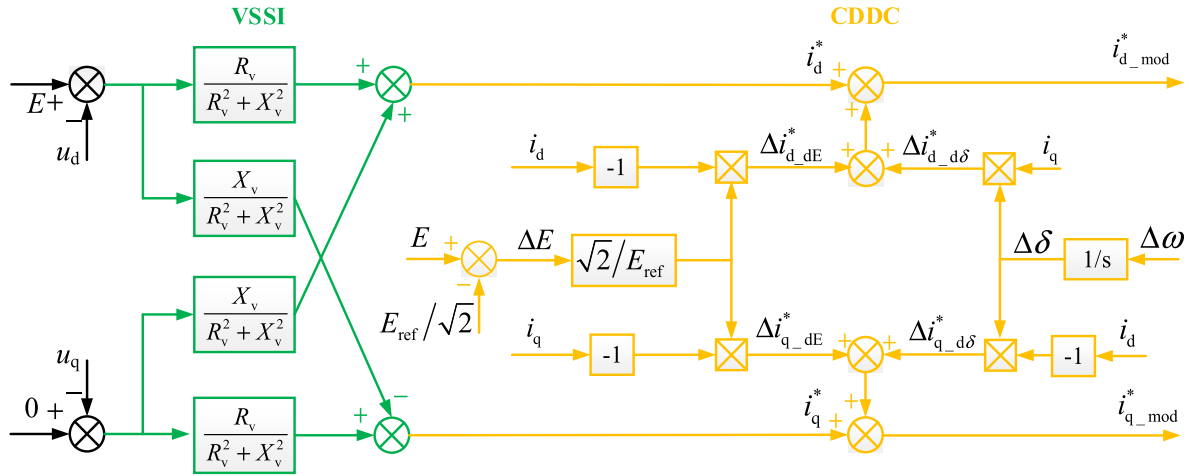


FIGURE 4. The control scheme of the proposed enhanced power decoupling strategy.

the VSG system is modelled by a dq-frame Norton equivalent circuit and the output currents are calculated as

$$\begin{bmatrix} i_d \\ i_q \end{bmatrix} = \mathbf{G}_i(s) \begin{bmatrix} i_{d_mod}^* \\ i_{q_mod}^* \end{bmatrix} + \mathbf{Z}_{odq}^{-1}(s) \begin{bmatrix} u_d \\ u_q \end{bmatrix} \quad (10)$$

where $\mathbf{G}_i(s)$ is the current gain matrix, $i_{d_mod}^*$ and $i_{q_mod}^*$ are the d - and q -axis current references respectively, u_d and u_q are the d - and q -axis components of voltage at PCC, s is the Laplace operator. $\mathbf{Z}_{odq}(s)$ is the output impedance that satisfies

$$\mathbf{Z}_{odq}(s) = \mathbf{Y}_{odq}^{-1}(s) = \begin{bmatrix} Z_{dd}(s) & Z_{dq}(s) \\ Z_{qd}(s) & Z_{qq}(s) \end{bmatrix} = \begin{bmatrix} Z_{dd}(s) & -Z_{qd}(s) \\ Z_{qd}(s) & Z_{dd}(s) \end{bmatrix} \quad (11)$$

In practice, the voltage feedforward plays an important role in reshaping the output impedance, which is discussed here. The output impedances with voltage feedforward (VSSI-1), denoted as Z_{dd_1} and Z_{qd_1} , and without voltage feedforward (VSSI-2), denoted as Z_{dd_2} and Z_{qd_2} , are shown as follows.

$$\begin{aligned} Z_{dd_1} &= G_h R_v = \frac{L_1 s^2 + (R_1 + k_{cp})s + k_{ci}}{k_{cp}s + k_{ci}} \cdot R_v \end{aligned} \quad (12)$$

$$\begin{aligned} Z_{qd_1} &= G_h X_v = \frac{L_1 s^2 + (R_1 + k_{cp})s + k_{ci}}{k_{cp}s + k_{ci}} \cdot X_v \end{aligned} \quad (13)$$

$$\begin{aligned} Z_{dd_2} &= \frac{[L_1 s^2 + (k_{cp} + R_1)s + k_{ci}][k_{cp}R_v + R_v^2 + X_v^2]s + k_{ci}R_v}{(k_{cp}^2 + 2k_{cp}R_v + R_v^2 + X_v^2)s^2 + (2k_{cp}k_{ci} + 2k_{ci}R_v)s + k_{ci}^2} \end{aligned} \quad (14)$$

$$\begin{aligned} Z_{qd_2} &= \frac{[L_1 s^2 + (k_{cp} + R_1)s + k_{ci}][k_{cp}X_v s + k_{ci}X_v]}{(k_{cp}^2 + 2k_{cp}R_v + R_v^2 + X_v^2)s^2 + (2k_{cp}k_{ci} + 2k_{ci}R_v)s + k_{ci}^2} \end{aligned} \quad (15)$$

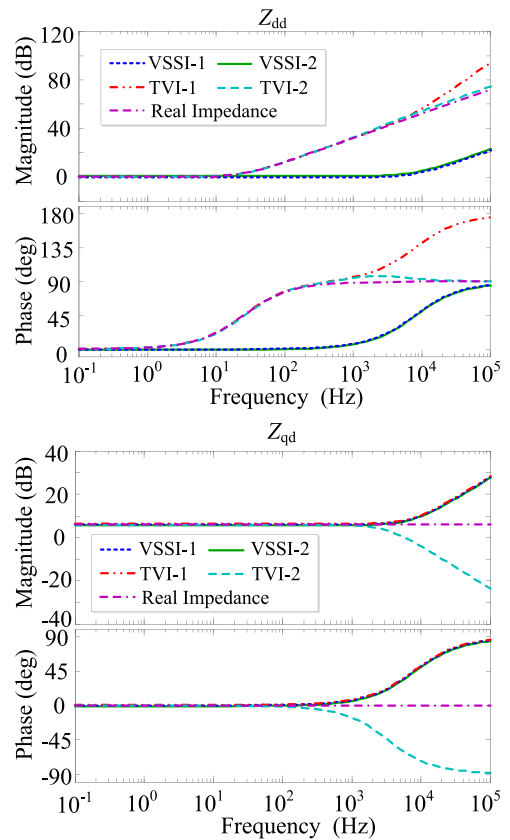


FIGURE 5. Bode diagrams of equivalent output impedance of $Z_{dd}(s)$ and $Z_{qd}(s)$.

where k_{cp} and k_{ci} are the proportional and integral coefficients of PI controller of current loop, L_1 and R_1 are the connection inductance and resistance.

Obviously, Z_{dd_2} and Z_{qd_2} have more complex forms than Z_{dd_1} and Z_{qd_1} . Z_{dd_1} and Z_{qd_1} are equal to the given impedance values multiplied by a transient transfer function

$G_h(s)$, and $G_h(s)|_{s=0} = 1$, which means that the DC output impedance in d - q reference frame (namely, the output impedance at nominal frequency (50Hz) in stationary abc reference frame) is totally determined by the given virtual impedance and independent of the controller and output filter parameters.

The bode diagrams of equivalent output impedances of VSSI-1 and VSSI-2 can be drawn in Fig. 5 according to (12)-(15). Likewise, for the purpose of comparative analysis, the bode diagrams of equivalent real physical impedance model, traditional virtual impedance method with voltage feedforward (TVI-1) and traditional virtual impedance method without voltage feedforward (TVI-2) are also drawn in Fig. 5. The setting value of resistance and reactance are all 1Ω and 2Ω .

It can be seen from the bode plots, in the low-frequency range, all the curves coincide with each other, which indicates that the VSSI can guarantee the pre-designed output impedance characteristics at the nominal frequency and its vicinity, and void the influence of filter and controller parameters. Therefore, for the purpose of optimal decoupling performance, the purely inductive output impedance can be realized directly by setting $R_v = 0$ in VSSI.

In the high frequency region, Z_{dd} of TVI-1 are larger than equivalent real inductance in magnitude and lead 90° in phase. Z_{dd} of TVI-2 are almost the same with the equivalent real inductance in magnitude and phase. Differently, Z_{dd} of VSSI-1 and VSSI-2 are both smaller than the equivalent real inductance in magnitude and have the same phase with the equivalent real inductance. It implies that the VSSI strategy lowers the high-frequency output impedance, reduces the harmonic voltage drop in output impedance caused by a disturbance of nonlinear loads, and thus improves the anti-disturbance capability.

B. CDDC PART

The VSSI strategy presented in Section III.A ensures the inductive output impedance to eliminate the power coupling caused by the existence of line impedance ratio R/X . After that, (3) can be simplified as

$$P = EU/X_v \cdot \sin \delta \quad (16)$$

$$Q = EU/X_v \cdot \cos \delta - U^2/X_v \quad (17)$$

Linearizing (16) and (17) at the steady-state operating point (E_0, δ_0) yields

$$\begin{bmatrix} \Delta P \\ \Delta Q \end{bmatrix} = \frac{U}{X_v} \begin{bmatrix} E_0 \cos \delta_0 & \sin \delta_0 \\ -E_0 \sin \delta_0 & \cos \delta_0 \end{bmatrix} \begin{bmatrix} \Delta \delta \\ \Delta E \end{bmatrix} \quad (18)$$

1) Q-DECOUPLING

Letting $\Delta Q = 0$ in (18), yields

$$\Delta E = (E_0 \sin \delta_0 / \cos \delta_0) \cdot \Delta \delta \quad (19)$$

where ΔE represents the error of virtual inner voltage caused by the power angle disturbance. Thus if ΔE can be compensated as (19), the coupling effect on reactive power can

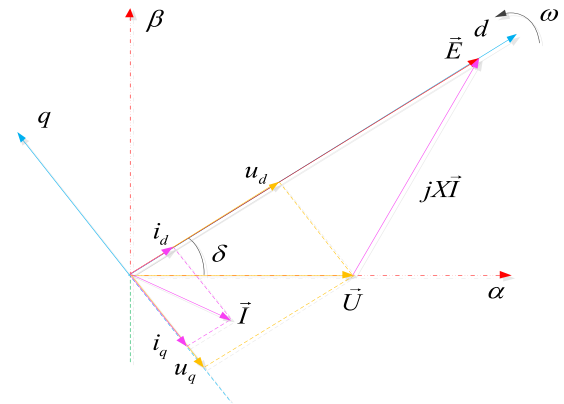


FIGURE 6. Phasor diagram of the equivalent circuit of grid-connected VSG.

be eliminated. Based on this idea, a novel current dynamic decoupling compensation (CDDC) method for the purpose of relaxing small power angle condition is presented, which is derived as following process.

The phasor diagram of the equivalent circuit of grid-connected VSG is shown in Fig. 6.

According to the phasor diagram, the d - and q - components of grid voltage are represented respectively as

$$\begin{cases} u_d = U \cos \delta \\ u_q = -U \sin \delta \end{cases} \quad (20)$$

The d - and q - components of output current are given by

$$i_d = (e_q - v_q)/X_v = U/X_v \cdot \sin \delta \quad (21)$$

$$i_q = -(e_d - v_d)/X_v = (U \cos \delta - E)/X_v \quad (22)$$

Linearizing (21) and (22) at (E_0, δ_0) , yields

$$\Delta i_d = U \cos \delta_0 / X_v \cdot \Delta \delta \quad (23)$$

$$\Delta i_q = -1/X_v \cdot \Delta E - U \sin \delta_0 / X_v \cdot \Delta \delta \quad (24)$$

The expressions of output active power and reactive power can be written as

$$\begin{cases} P = u_d i_d + u_q i_q \\ Q = u_q i_d - u_d i_q \end{cases} \quad (25)$$

The small signal models in terms of current variable are given by

$$\begin{cases} \Delta P = u_{d0} \Delta i_d + u_{q0} \Delta i_q \\ \Delta Q = u_{q0} \Delta i_d - u_{d0} \Delta i_q \end{cases} \quad (26)$$

Expression (27) and (28) can be derived from (23) and (24) respectively,

$$\Delta \delta = (X_v / U \cos \delta_0) \Delta i_d \quad (27)$$

$$\Delta E = -X_v \Delta i_q - U \sin \delta_0 \Delta \delta \quad (28)$$

Substituting (19), (20), (25) and (27) into (28) gives

$$-u_{d0} (-i_{d0} \Delta \delta) + u_{q0} i_{q0} \Delta \delta = -u_{d0} \Delta i_q + u_{q0} \Delta i_d \quad (29)$$

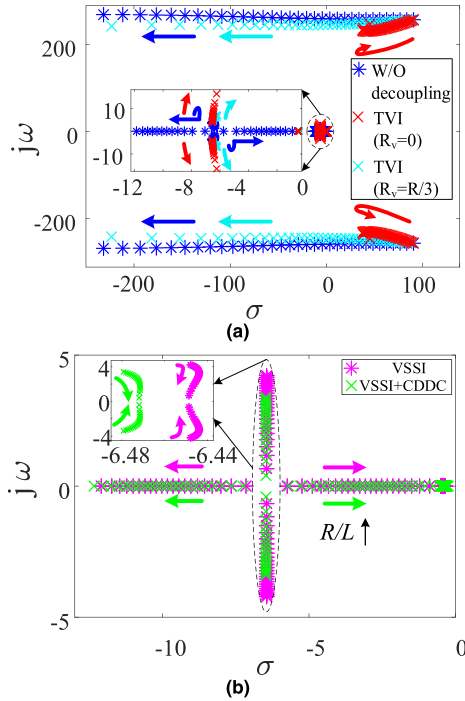


FIGURE 7. Characteristic root locus of \mathbf{A} when R/X varies from 0 to infinity with $|Z_v| = 8.9 \Omega$ (a) W/O decoupling and TVI with different R_v , (b) VSSI and VSSI+CDDC.

Equation (29) shows that the error ΔQ caused by the undesired coupling can be eliminated if the output current is changed from (i_{d0}, i_{q0}) to $(i_{d0} + i_{q0} \cdot \Delta\delta, i_{q0} - i_{d0} \cdot \Delta\delta)$. Therefore, the current compensation references for Q - δ decoupling are designed as

$$\begin{cases} \Delta i_{d_d\delta}^* = i_q \cdot \Delta\delta (a) \\ \Delta i_{q_d\delta}^* = -i_d \cdot \Delta\delta (b) \end{cases} \quad (30)$$

2) P-DECOUPLING

According to (18), at the initial operating point (E_0, δ_0) , the active power error caused by voltage disturbance is written as

$$\Delta P = (U \sin \delta_0 / X_v) \cdot \Delta E = (P_0 / E_0) \cdot \Delta E \quad (31)$$

Assuming that the corresponding d - and q - components of output current error caused by the disturbance of voltage ΔE are Δi_d and Δi_q , combining (26) with (31) yields

$$\begin{aligned} & u_{d0} \Delta i_{d_dE}^* + u_{q0} \Delta i_{q_dE}^* \\ &= -\Delta P = -P_0 / E_0 \cdot \Delta E = -\frac{u_{d0} i_{d0} + u_{q0} i_{q0}}{E_0} \Delta E \\ &= u_{d0} \left(-\frac{i_{d0}}{E_0} \Delta E \right) + u_{q0} \left(-\frac{i_{q0}}{E_0} \Delta E \right) \end{aligned} \quad (32)$$

where i_{d0} and i_{q0} are the steady-state value of output current.

Therefore, the current feedforward reference for P - E decoupling

$$\begin{cases} \Delta i_{d_dE}^* = -i_{d0} / E_0 \cdot \Delta E (a) \\ \Delta i_{q_dE}^* = -i_{q0} / E_0 \cdot \Delta E (b) \end{cases} \quad (33)$$

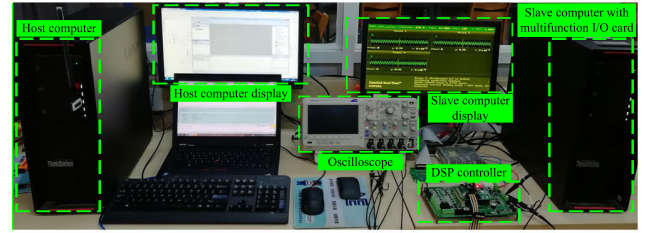


FIGURE 8. The platform of hardware-in-the-loop experiments.

TABLE 1. Main parameters for VSG system.

Symbol	Quantity	Value
E_{ref}	nominal voltage amplitude of virtual inner voltage	311 V
ω_{ref}	nominal radian frequency	100π rad/s
P_n	nominal power	10 kW
f_s	switching frequency	10 kHz
X_L	connection reactance	0.3 p.u.
J	virtual inertia	1 N·m
D	damping coefficient	80 p.u.
k_P	active power droop coefficient	1.6 kW/Hz
k_Q	reactive power droop coefficient	0.45 kVar/V

To make it easier to obtain the P - E decoupling compensation current reference, the voltage steady-state value can be replaced with voltage reference. Then, combining (30) and (33), the modified current reference is designed as

$$i_{d_mod}^* = i_d^* + \Delta i_{d_d\delta}^* + \Delta i_{d_dE}^* = i_d^* + i_q \cdot \Delta\delta - i_d / E_{ref} \cdot \Delta E \quad (34)$$

$$i_{q_mod}^* = i_q^* + \Delta i_{q_d\delta}^* + \Delta i_{q_dE}^* = i_q^* - i_d \cdot \Delta\delta - i_q / E_{ref} \cdot \Delta E \quad (35)$$

It can be seen from (34) and (35), the calculation of feedforward compensation only needs to measure the real-time operating state, i.e. current, power angle, but does not depend on the parameters which can hardly measure accurately, e.g. line impedance, etc. Therefore, the proposed strategy can realize the accurate decoupling theoretically and are well robust to the variation of parameters.

IV. DYNAMIC PERFORMANCE AND STABILITY ANALYSIS FOR ENHANCED VSG STRATEGY

In order to study the effectiveness and characteristics of the proposed decoupling strategy, a small signal model in state space for the whole VSG system shown in Fig. 1 is also built.

Linearized small signal model can be expressed as

$$\Delta \dot{\mathbf{x}} = \mathbf{A} \cdot \Delta \mathbf{x} + \mathbf{B} \cdot \Delta \mathbf{u} \quad (36)$$

$$\Delta \mathbf{y} = \mathbf{C} \cdot \Delta \mathbf{x} + \mathbf{D} \cdot \Delta \mathbf{u} \quad (37)$$

where \mathbf{A} , \mathbf{B} , \mathbf{C} , \mathbf{D} are shown in Appendix and the state vector, input vector and output vector are given by

$$\Delta \mathbf{x} = [\Delta Q_f \Delta P_f \Delta i_d \Delta i_q \Delta \omega \Delta \delta \Delta \gamma_d \Delta \gamma_q]^T \quad (38)$$

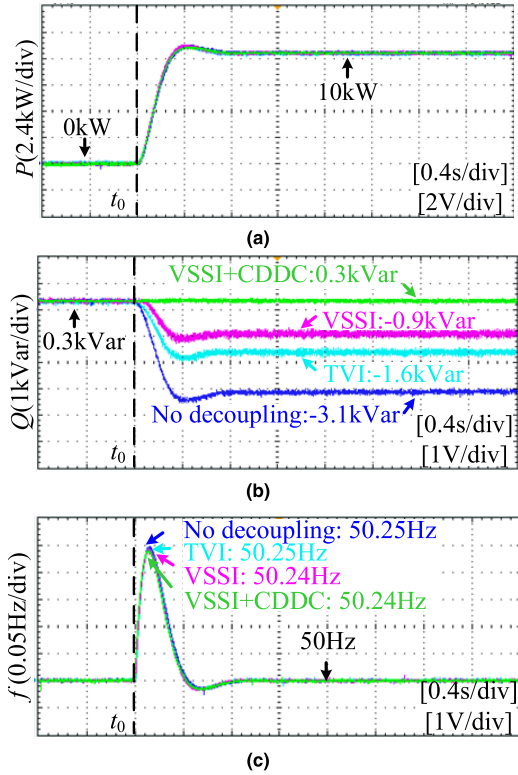


FIGURE 9. Responses to active power reference step respectively under four different control strategies with R/X as 0.25. (a) active power, (b) reactive power, (c) output frequency.

$$\Delta \mathbf{u} = [\Delta Q_{ref} \ \Delta E_{ref} \ \Delta P_{ref} \ \Delta \omega_g \ \Delta u]^T \quad (39)$$

$$\Delta \mathbf{y} = [\Delta Q \ \Delta P]^T \quad (40)$$

where $\Delta \gamma_d$ is the small signal of integral of current difference between $i_{d_mod}^*$ and i_d , and $\Delta \gamma_q$ is that between $i_{q_mod}^*$ and i_q .

Then, the transfer function matrix can be derived as

$$\mathbf{G}(s) = \mathbf{C} (s\mathbf{I} - \mathbf{A})^{-1} \mathbf{B} + \mathbf{D} \quad (41)$$

where $\mathbf{G}(s)$ is a 2×5 matrix. $G_{11}(s)$ and $G_{23}(s)$ are the closed loop transfer functions from reactive power reference to output reactive power and from active power reference to output active power, namely $\Delta Q(s)/\Delta Q_{ref}(s)$ and $\Delta P(s)/\Delta P_{ref}(s)$, which describe the response characteristics of P -control and Q -control. And the power coupling effect is described by $\Delta Q(s)/\Delta P_{ref}(s)$ and $\Delta P(s)/\Delta Q_{ref}(s)$, corresponding to $G_{13}(s)$ and $G_{21}(s)$ of $\mathbf{G}(s)$, which indicates the reactive power response to active power reference change and active power response to reactive power reference change.

The characteristic root locus diagrams of \mathbf{A} in constant impedance magnitude but different impedance ratio are shown in Fig. 7, where only the locus of dominant poles is drawn.

It can be seen from Fig. 7 (a), when no decoupling method is adopted, there are two poles located at right half plane at small impedance ratio, which means the system is unstable under very small impedance ratio without any decoupling

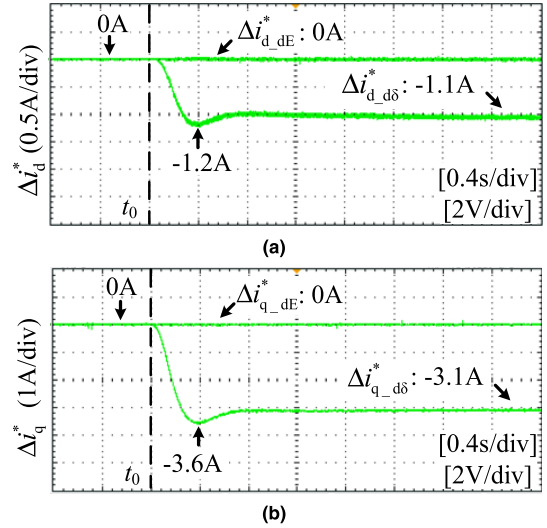


FIGURE 10. Feedforward decoupling current references in VSSI+CDDC during response to active power reference step (a) in d axis, (b) in q axis.

strategy. Along with the increase of impedance ratio, these two poles move to left half plane gradually and the system becomes stable. However, these two poles are still conjugate poles and are underdamped over a wide range of impedance ratios. Meanwhile, there are four poles that are close to imaginary axis but always stay at left half plane. When the TVI is adopted with $R_v = 0\Omega$, there are two poles always moving at right half plane. That means the system cannot be stable if TVI is adopted with $R_v = 0\Omega$. Nevertheless, when the TVI is adopted with $R_v = R/3$, these two poles are located at right half plane at very small impedance ratio but move to left half plane along with the increase of R/X . That means the system stability increases and the damping of these two poles increases along with the increase of R/X when TVI is adopted with R_v larger than 0. By the contrast between root locus without decoupling and the root locus with TVI, it can be found that R_v smaller than R brings weaker damping to those two poles under TVI. However, to weaken the power coupling, R_v should be set as a value smaller than R . Therefore, oscillation may occur during dynamic process due to those two poles in TVI.

When VSSI is adopted, thanks to the unique characteristic of VSSI that the value of virtual reactance does not increase with frequency, \mathbf{A} under the VSSI strategy is two orders less than that under the TVI strategy. As a result, as shown in Fig. 7 (b), those two unstable roots do not exist under VSSI, so all the poles under VSSI only move at left half plane and the system is stable with any impedance ratio. It is demonstrated that the VSSI can improve the system stability more effectively than the strategy without decoupling and TVI. In addition, without the limitation of the two poles at right half plane, R_v in VSSI can be set to 0, which is helpful to give VSSI better decoupling effect than TVI. In Fig. 7 (b), when the VSSI and CDDC are adopted at the same time, as shown in the diagram of conjugate roots locus that is zoomed in,

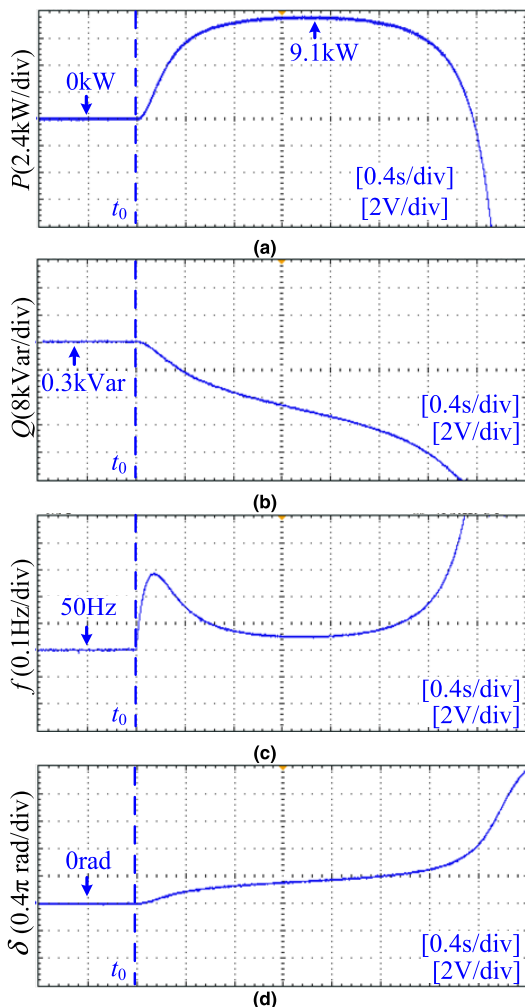


FIGURE 11. Responses to active power reference step without power decoupling with R/X as 1. (a) active power, (b) reactive power, (c) frequency, (d) power angle.

the damping of the two conjugate roots are further increased, which demonstrates that the proposed VSSI+CDDC strategy can not only improve the system stability but also benefit the dynamic response of the system.

V. EXPERIMENTAL RESULTS

The experiments are conducted in the hardware-in-the-loop platform as shown in Fig. 8 to verify the effectiveness and superiority of the proposed enhanced decoupling strategy. The main circuit is simulated by real time simulation in the slave computer while the control algorithm runs in the core controller of TMS320F28335 DSP. The data transition between them is implemented by a multifunction I/O card MF624 that is embedded in the slave computer. The topology is the same with that in Fig. 2. but the DGs are replaced by a constant voltage DC source with 700V. Four control strategies, i.e. VSG strategy without decoupling strategy, TVI based decoupling strategy, only the proposed VSSI based decoupling strategy and the proposed VSSI with

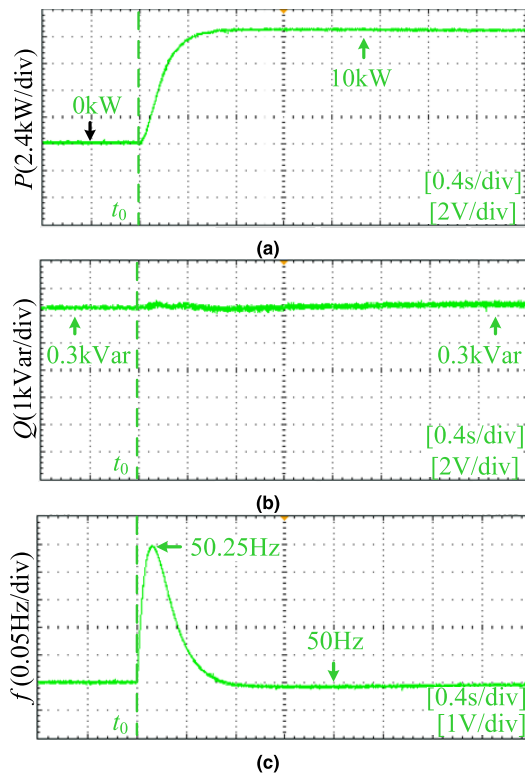


FIGURE 12. Responses to active power reference step with VSSI+CDDC with R/X as 1. (a) active power, (b) reactive power, (c) frequency.

CDDC strategy, are adopted respectively in the system with the same main parameters listed in Table 1.

A. COMPARATIVE EXPERIMENTS OF Q-DECOUPLING PERFORMANCE

When $t < t_0$, VSG operates steadily with $P = 0$ and $Q = 300\text{Var}$. the response to active power reference step at t_0 with the value of R/X as 0.25 is shown in Fig. 9. The data is calculated by DSP according to the control algorithm and the measured voltage and current from the main circuit, and converted to analog signal by MF624 then displayed on the oscilloscope.

In Fig. 9 (b), when no decoupling methods are adopted, the reactive power output exhibits an unwanted descent to -3.4kVar and reaches a new steady-state value of -3.1kVar. That means -3.4pu steady-state deviation of reactive power is generated by the active power step because of the coupling impact from active power loop. Such large deviation of reactive power brings great overcurrent risk, which is very necessary to avoid.

When the TVI method is added, the power coupling weakens markedly. However, as analysed in Section IV, zero virtual resistance in TVI will destabilize the system. The virtual resistance in TVI thus can be set as a smaller value than real line resistance but not zero. Then the power coupling caused by nonzero impedance ratio still exists but is weakened than that with no decoupling method. Thus, the impact of active

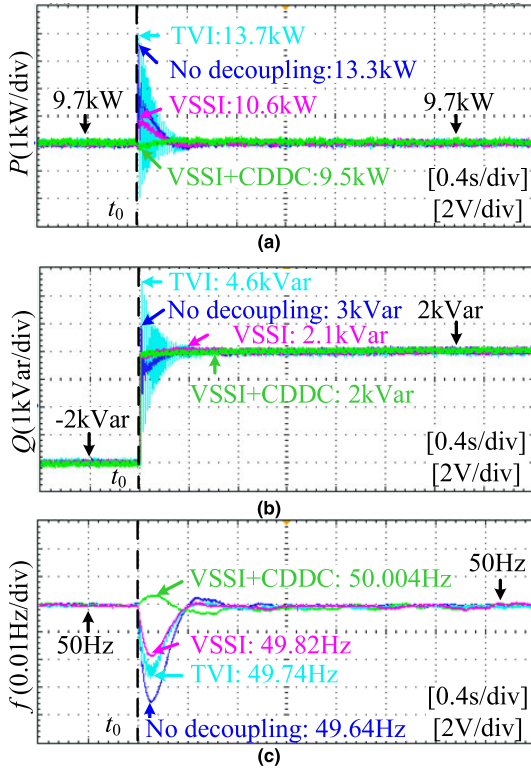


FIGURE 13. Responses to reactive power reference step respectively under four different control strategies (a)active power (b)reactive power (c) output frequency.

power step change on reactive power output is still obvious. Under the circumstance, the minimum value of reactive power is -1.8kVar and new steady-state value is -1.6kVar . The steady-state deviation of reactive power is -1.9pu .

When only the proposed VSSI is added, the virtual resistance can be set to 0, which gives the VSSI better effect on weakening the power coupling caused by line impedance. Then the deviation of reactive power is decreased to -0.9kVar . But the power coupling caused by the nonzero power angle is not complemented yet, which leads the reactive power to deviate from initial value -1.2kVar .

As shown in Fig. 9 (b), when the proposed VSSI and CDDC operate simultaneously, the deviation of reactive power during the whole process almost disappears. The main reason for such excellent performance is that the feedforward decoupling currents, $\Delta i_{d,d\delta}^*$ and $\Delta i_{q,d\delta}^*$ are adjusted according to the change of power angle along with the active power change as shown in Fig. 10.

As a result, the phase and amplitude of the inverter are adjusted at the same time to maintain reactive power unchanged while active power follows the reference accurately. Q -coupling problem is addressed better. It proves that the proposed method in this paper can eliminate the steady-state error of reactive power and enable VSG to output reactive power in strict accordance with the requirement of the reactive power control loop regardless of the influence of the active power control loop.

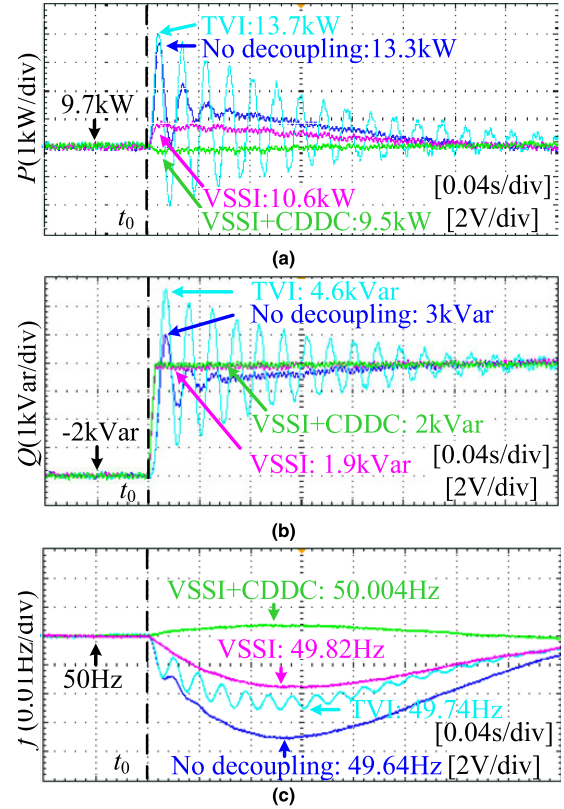


FIGURE 14. Zoom-in responses to reactive power reference step respectively under four different control strategies (a)active power (b)reactive power (c) output frequency.

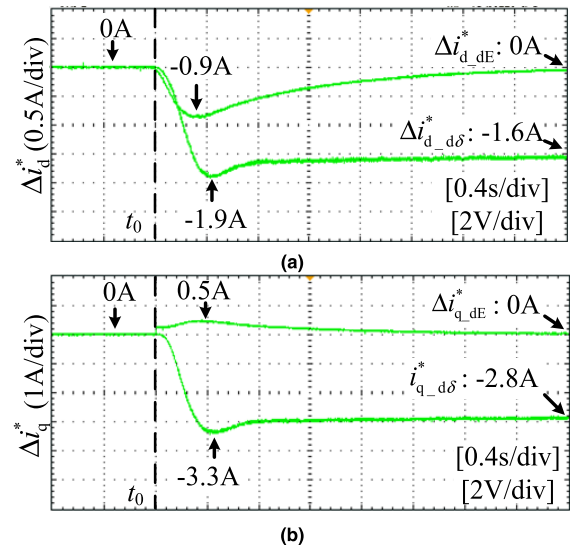


FIGURE 15. Feedforward decoupling current references in VSSI+CDDC during response to reactive power reference step (a) in d axis, (b) in q axis.

When the impedance ratio R/X is larger, the power coupling will be more serious. As shown in Fig. 11, with the impedance ratio as 1, the power angle diverges due to serious power coupling when the active power reference steps, and the system even destabilized without decoupling strategy.

Fortunately, when the proposed VSSI+CDDC decoupling strategy is adopted under the same circumstances, the system can respond to the active power reference step stably as shown in Fig. 12. And the reactive power almost maintains unchanged during the active power step response. It demonstrates the proposed strategy can achieve power decoupling effectively and benefit the system stability.

B. COMPARATIVE EXPERIMENTS OF P-DECOUPLING PERFORMANCE

The reactive power reference is set properly to make output reactive power of VSG produce a step ascent of 4kVar at t_0 and the responses under circumstances of the four different control strategies are shown in Fig. 13 and zoomed in as shown in Fig. 14.

In Fig. 13. (a) and Fig. 14. (a), under circumstance of basic VSG strategy without any decoupling method, obvious shock and oscillatory are shown in active power, which does not agree with the pre-designed dynamic characteristics. The reason is that the change of reactive power reference transmits to the active power through power coupling channels. Then the

adjustment of active power loop in turn affect the adjustment of reactive power, which leads to slower response of reactive power as shown in Fig. 13. (b) and Fig. 14. (b).

Under circumstance of TVI, smaller virtual resistance is set to weaken the power coupling caused by large line impedance ratio. The fluctuation of frequency is smaller than that without any decoupling methods as shown in Fig. 13. (c) and Fig. 14. (c). It indicates that the low frequency component of the active power fluctuation caused by the reactive step decreases, which means TVI indeed weakens the power coupling lightly. However, smaller resistance leads to weaker damping effect at the same time, which makes the high frequency oscillation more serious as shown in Fig. 13. That is in accordance with the analysis in Section IV.

When only the proposed VSSI is adopted, the virtual resistance can be set as 0, which weakens the coupling caused by large impedance ratio effectively. Thanks to the unique characteristic of VSSI, damping of the system is still enough with zero virtual resistance, so oscillation is restrained effectively. So the shock and oscillation in active power is restrained obviously as shown in Fig. 13. (a) and Fig. 14. (a), and the reactive

$$A = \begin{bmatrix} -\omega_f & 0 & \frac{3\omega_f U_{d0}}{2} & \frac{3\omega_f U_{d0}}{2} & 0 & \frac{3\omega_f I_{d0} U_{d0} + 3\omega_f I_{q0} U_{q0}}{2} & 0 & 0 \\ 0 & -\omega_f & \frac{3}{2}\omega_f U_{d0} & \frac{3}{2}\omega_f U_{q0} & 0 & \frac{3}{2}\omega_f (I_{d0} U_{q0} - U_{d0} I_{q0}) & 0 & 0 \\ \frac{N \frac{I_d}{e_{ref}} k_p k_q - k_p R_v k_q / W}{L} & 0 & \frac{N}{e_{ref}} k_p k_q (Q_{m0} - Q_{ref0}) - k_p - R_{line} & \frac{M k_p \delta_0 - \omega_s L + \omega L_{line}}{L} & 0 & \frac{M k_p I_q + (-R_v U_{q0} + \omega_s L_v U_{d0}) k_p / W - U_{q0}}{L} & k_i / L & 0 \\ \frac{Z \frac{I_q}{e_{ref}} k_p k_q + \omega_s L_v k_p k_q / W}{L} & 0 & \frac{-M k_p \delta_0 + \omega_s L - \omega L_{line}}{L} & \frac{Z}{e_{ref}} k_p k_q (Q_{m0} - Q_{ref0}) - k_p - R_{line} & 0 & \frac{-M k_p I_d + (\omega_s L_v U_{q0} + R_v U_{d0}) k_p / W + U_{d0}}{L} & 0 & k_i / L \\ 0 & -1/T & 0 & 0 & \frac{K_p + D}{T} & 0 & 0 & 0 \\ 0 & 0 & 0 & 0 & 1 & 0 & 0 & 0 \\ N \frac{I_d}{e_{ref}} k_q - R_v k_q / W & 0 & \frac{N}{e_{ref}} k_q (Q_{m0} - Q_{ref0}) - 1 & M \delta_0 & 0 & M I_q + (-R_v U_{q0} + \omega_s L_v U_{d0}) / W & 0 & 0 \\ Z \frac{I_q}{e_{ref}} k_q + \omega_s L_v k_q / W & 0 & -M \delta_0 & \frac{Z}{e_{ref}} k_q (Q_{m0} - Q_{ref0}) - 1 & 0 & -M I_d + (\omega_s L_v U_{q0} + R_v U_{d0}) / W & 0 & 0 \end{bmatrix}$$

$$B = \begin{bmatrix} 0 & 0 & 0 & 0 & 0 & -\frac{3}{2}\omega_f (I_{d0} \sin \delta_0 + I_{q0} \cos \delta_0) & & \\ 0 & 0 & 0 & 0 & 0 & \frac{3}{2}\omega_f (I_{d0} \cos \delta_0 - I_{q0} \sin \delta_0) & & \\ \frac{R_v k_p k_q}{WL} - N \frac{I_d}{Le_{ref}} k_p k_q & & \frac{R_v k_p}{WL} & 0 & 0 & \frac{-k_p R_v \cos \delta_0 + k_p \omega_s L_v \sin \delta_0}{WL} - \frac{\cos \delta_0}{L} & & \\ \frac{-\omega_s L_v k_p k_q}{WL} - Z \frac{I_q}{Le_{ref}} k_p k_q & & \frac{-\omega_s L_v k_p}{WL} & 0 & 0 & \frac{k_p \omega_s L_v \cos \delta_0 + k_p R_v \sin \delta_0}{WL} + \frac{\sin \delta_0}{L} & & \\ 0 & 0 & 0 & \frac{1}{T} & 0 & 0 & & \\ 0 & 0 & 0 & 0 & -1 & 0 & & \\ \frac{R_v k_q}{W} - N \frac{I_d}{e_{ref}} k_q & & \frac{R_v}{W} & 0 & 0 & \frac{-R_v \cos \delta_0 + \omega_s L_v \sin \delta_0}{W} & & \\ \frac{-\omega_s L_v k_q}{W} - Z \frac{I_q}{e_{ref}} k_q & & \frac{-\omega_s L_v}{W} & 0 & 0 & \frac{\omega_s L_v \cos \delta_0 + R_v \sin \delta_0}{W} & & \end{bmatrix}$$

$$C = \begin{bmatrix} 0 & 0 & \frac{3}{2}U_{q0} & -\frac{3}{2}U_{d0} & 0 & -\frac{3}{2}(I_{d0}U_{d0} + I_{q0}U_{q0}) & 0 & 0 \\ 0 & 0 & \frac{3}{2}U_{d0} & \frac{3}{2}U_{q0} & 0 & \frac{3}{2}(I_{d0}U_{q0} - I_{q0}U_{d0}) & 0 & 0 \end{bmatrix}$$

$$D = \begin{bmatrix} 0 & 0 & 0 & 0 & -\frac{3}{2}(I_{d0} \sin \delta_0 + I_{q0} \cos \delta_0) \\ 0 & 0 & 0 & 0 & \frac{3}{2}(I_{d0} \cos \delta_0 - I_{q0} \sin \delta_0) \end{bmatrix}$$

power reaches steady-state value rapidly without oscillation Fig. 13. (b) and Fig. 14. (b). However, due to the coupling caused by power angle that is not complemented, 0.9kW shock is still generated in active power (see Fig. 14. (a)) and frequency fluctuation is caused as a result (see Fig. 14. (c)). Nevertheless, no oscillation or shock should be observed in the ideal response of active power during the whole process.

When the proposed VSSI + CDDC strategy is added, the ideal response is realized. As shown in Fig. 15, the feedforward decoupling currents are adjusted rapidly at the moment that reactive power is adjusted, so the phase and amplitude of output voltage are changed at the same time to maintain unchanged active power and realize the expected reactive power. As shown in Fig. 13, active power has been shielded from the effects of reactive power, and reactive power reaches the steady-state value rapidly, which indicates that the proposed VSSI+CDDC weakens the coupling caused by both large impedance ratio and power angle effectively.

VI. CONCLUSION

Power coupling issue of VSG can produce output power error, amplify power oscillation and influence the system stability. In this paper, the power coupling characteristics of VSG have been analysed, and an enhanced power decoupling method by using virtual steady-state synchronous impedance and current dynamic decoupling compensation has been proposed. This method can eliminate the coupling effect caused by the high line impedance ratio and nonzero power angle at the same time. In the meanwhile, the output impedance and its characteristics analysis of improved VSG strategy are presented. Then, the state space models of traditional VSG and improved VSG strategy are built. Through comparative analysis, it is proved that the proposed enhanced decoupling method can mitigate the power coupling more effectively. In addition, the stability of VSG system is enhanced. Finally, the experimental results demonstrate that the proposed method can eliminate the steady-state error of output power, alleviate the power oscillation, and improve the dynamic and steady-state responses of active power and reactive power. This method can also be transplanted to the other droop-based control strategies.

APPENDIX

See appendix equation as shown at the bottom of previous page.

REFERENCES

- [1] S. Rahman, "Green power: What is it and where can we find it?" *IEEE Power Energy Mag.*, vol. 1, no. 1, pp. 30–37, Jan. 2003.
- [2] F. Blaabjerg, Z. Chen, and S. B. Kjaer, "Power electronics as efficient interface in dispersed power generation systems," *IEEE Trans. Power Electron.*, vol. 19, no. 5, pp. 1184–1194, Sep. 2004.
- [3] J. M. Carrasco, L. G. Franquelo, J. T. Bialasiewicz, E. Galvan, R. C. PortilloGuisado, M. A. M. Prats, J. I. Leon, and N. Moreno-Alfonso, "Power-electronic systems for the grid integration of renewable energy sources: A survey," *IEEE Trans. Ind. Electron.*, vol. 53, no. 4, pp. 1002–1016, Jun. 2006.
- [4] L. Xiong, X. Liu, C. Zhao, and F. Zhuo, "A fast and robust real-time detection algorithm of decaying DC transient and harmonic components in three-phase systems," *IEEE Trans. Power Electron.*, vol. 35, no. 4, pp. 3332–3336, Apr. 2020.
- [5] Q.-C. Zhong, "Power-electronics-enabled autonomous power systems: Architecture and technical routes," *IEEE Trans. Ind. Electron.*, vol. 64, no. 7, pp. 5907–5918, Jul. 2017.
- [6] J. Driesen and K. Visscher, "Virtual synchronous generators," in *Proc. IEEE Power Energy Soc. Gen. Meeting-Convers. Del. Electr. Energy 21st Century*, Jul. 2008, pp. 1–3.
- [7] T. Shintai, Y. Miura, and T. Ise, "Oscillation damping of a distributed generator using a virtual synchronous generator," *IEEE Trans. Power Del.*, vol. 29, no. 2, pp. 668–676, Apr. 2014.
- [8] Y. Ma, W. Cao, L. Yang, F. F. Wang, and L. M. Tolbert, "Virtual synchronous generator control of full converter wind turbines with short-term energy storage," *IEEE Trans. Ind. Electron.*, vol. 64, no. 11, pp. 8821–8831, Nov. 2017.
- [9] J. Liu, Y. Miura, and T. Ise, "Comparison of dynamic characteristics between virtual synchronous generator and droop control in inverter-based distributed generators," *IEEE Trans. Power Electron.*, vol. 31, no. 5, pp. 3600–3611, May 2016.
- [10] L. Xiong, F. Zhuo, F. Wang, X. Liu, Y. Chen, M. Zhu, and H. Yi, "Static synchronous generator model: A new perspective to investigate dynamic characteristics and stability issues of grid-tied PWM inverter," *IEEE Trans. Power Electron.*, vol. 31, no. 9, pp. 6264–6280, Sep. 2016.
- [11] H. Alatrash, A. Mensah, E. Mark, G. Haddad, and J. Enslin, "Generator emulation controls for photovoltaic inverters," *IEEE Trans. Smart Grid*, vol. 3, no. 2, pp. 996–1011, Jun. 2012.
- [12] Y. Chen, R. Hesse, D. Turschner, and H.-P. Beck, "Improving the grid power quality using virtual synchronous machines," in *Proc. Int. Conf. Power Eng., Energy Electr. Drives (ICREPD)*, May 2011, pp. 1–6.
- [13] H.-P. Beck and R. Hesse, "Virtual synchronous machine," in *Proc. 9th Int. Conf. Electr. Power Qual. Utilisation (EPQU)*, Oct. 2007, pp. 1–6.
- [14] Q.-C. Zhong and G. Weiss, "Synchronverters: Inverters that mimic synchronous generators," *IEEE Trans. Ind. Electron.*, vol. 58, no. 4, pp. 1259–1267, Apr. 2011.
- [15] J. M. Guerrero, L. GarcıadeVicuna, J. Matas, M. Castilla, and J. Miret, "Output impedance design of parallel-connected UPS inverters with wireless load-sharing control," *IEEE Trans. Ind. Electron.*, vol. 52, no. 4, pp. 1126–1135, Aug. 2005.
- [16] H. Mahmood, D. Michaelson, and J. Jiang, "Accurate reactive power sharing in an islanded microgrid using adaptive virtual impedances," *IEEE Trans. Power Electron.*, vol. 30, no. 3, pp. 1605–1617, Mar. 2015.
- [17] M. Eskandari and L. Li, "Microgrid operation improvement by adaptive virtual impedance," *IET Renew. Power Gener.*, vol. 13, no. 2, pp. 296–307, Feb. 2019.
- [18] Y. Hu, Y. Shao, R. Yang, X. Long, and G. Chen, "A configurable virtual impedance method for grid-connected virtual synchronous generator to improve the quality of output current," *IEEE J. Emerg. Sel. Topics Power Electron.*, early access, May 22, 2019, doi: 10.1109/jestpe.2019.2918386.
- [19] K. De Brabandere, B. Bolsens, J. Van den Keybus, A. Woyte, J. Driesen, and R. Belmans, "A voltage and frequency droop control method for parallel inverters," *IEEE Trans. Power Electron.*, vol. 22, no. 4, pp. 1107–1115, Jul. 2007.
- [20] T. Wu, Z. Liu, J. Liu, S. Wang, and Z. You, "A unified virtual power decoupling method for droop-controlled parallel inverters in microgrids," *IEEE Trans. Power Electron.*, vol. 31, no. 8, pp. 5587–5603, Aug. 2016.
- [21] C. N. Rowe, T. J. Summers, R. E. Betz, D. J. Cornforth, and T. G. Moore, "Arctan power–frequency droop for improved microgrid stability," *IEEE Trans. Power Electron.*, vol. 28, no. 8, pp. 3747–3759, Aug. 2013.
- [22] Y. Li and Y. W. Li, "Power management of inverter interfaced autonomous microgrid based on virtual frequency-voltage frame," *IEEE Trans. Smart Grid*, vol. 2, no. 1, pp. 30–40, Mar. 2011.
- [23] X. Yan and Y. Zhang, "Power coupling analysis of inverters based on relative gain method and decoupling control based on feedforward compensation," in *Proc. Int. Conf. Renew. Power Gener. (RPG)*, 2015, pp. 1–5.
- [24] Z. Peng, J. Wang, Y. Wen, D. Bi, Y. Dai, and Y. Ning, "Virtual synchronous generator control strategy incorporating improved governor control and coupling compensation for AC microgrid," *IET Power Electron.*, vol. 12, no. 6, pp. 1455–1461, May 2019.

[25] Z. Peng, J. Wang, D. Bi, Y. Wen, Y. Dai, X. Yin, and J. Shen, "Droop control strategy incorporating coupling compensation and virtual impedance for microgrid application," *IEEE Trans. Energy Convers.*, vol. 34, no. 1, pp. 277–291, Mar. 2019.

[26] Y. Zhang and U. Raheja, "An optimized virtual synchronous generator control strategy for power decoupling in grid connected inverters," in *Proc. IEEE Energy Convers. Congr. Exposit. (ECCE)*, Baltimore, MD, USA, Sep. 2019, pp. 49–54.

[27] J. Liu, Y. Miura, H. Bevrani, and T. Ise, "Enhanced virtual synchronous generator control for parallel inverters in microgrids," *IEEE Trans. Smart Grid*, vol. 8, no. 5, pp. 2268–2277, Sep. 2017.

[28] X. Li, Y. Hu, Y. Shao, and G. Chen, "Mechanism analysis and suppression strategies of power oscillation for virtual synchronous generator," in *Proc. 43rd Annu. Conf. IEEE Ind. Electron. Soc. (IECON)*, Oct. 2017, pp. 4955–4960.

[29] D. Yang, H. Wu, X. Wang, and F. Blaabjerg, "Suppression of synchronous resonance for VSGs," *J. Eng.*, vol. 2017, no. 13, pp. 2574–2579, Jan. 2017.

[30] B. Li, L. Zhou, X. Yu, C. Zheng, and J. Liu, "Improved power decoupling control strategy based on virtual synchronous generator," *IET Power Electron.*, vol. 10, no. 4, pp. 462–470, Mar. 2017.

[31] E. Bristol, "On a new measure of interaction for multivariable process control," *IEEE Trans. Autom. Control*, vol. AC-11, no. 1, pp. 133–134, Jan. 1966.



YONGHUI LIU (Graduate Student Member, IEEE) received the B.S. degree in electrical engineering from the Harbin Institute of Technology, Heilongjiang, China, in 2013, and the M.S. degree in electrical engineering from Xi'an Jiaotong University, Xi'an, China, in 2016, where she is currently pursuing the Ph.D. degree in electrical engineering.

Her research interests include the modeling and control of converters, renewable energy integration, wireless power transfer, and VSC-HVDC.



NINGYI XU received the B.S. degree in electrical engineering from Central South University, China, in 2014, and the M.S. degree in electrical engineering from Xi'an Jiaotong University, Xi'an, China, in 2017.

He is currently working with State Grid Ningbo Electric Power Supply Company, Ltd., Ningbo, China. His research interests include the modeling and control of converters, and renewable energy integration.



MINGXUAN LI (Graduate Student Member, IEEE) received the B.S. degree in electrical engineering from Jilin University, Jilin, China, in 2012. He is currently pursuing the Ph.D. degree in electrical engineering with Xi'an Jiaotong University, Xi'an, China.

His research interests include renewable energy integration, the modeling and control of converters, stability analyses, and VSC-HVDC.



SIRUI SHU received the B.S. degree in electrical engineering from Xi'an Jiaotong University, Xi'an, China, in 2019, where she is currently pursuing the M.S. degree in electrical engineering.

Her research interests include the modeling and control of converters, and renewable energy integration.



YUE WANG (Member, IEEE) received the B.S. degree from Xi'an Jiaotong University, Xi'an, China, in 1994, the M.S. degree from Beijing Jiaotong University, Beijing, China, in 2000, and the Ph.D. degree from Xi'an Jiaotong University, in 2003, all in electrical engineering.

He is currently a Full Professor with the School of Electrical Engineering, Xi'an Jiaotong University. His research interests include renewable energy integration, wireless power transfer, active power filters, multilevel converters, and HVDC.



WANJUN LEI (Member, IEEE) received the B.S., M.S., and Ph.D. degrees in electrical engineering from Xi'an Jiaotong University, Xi'an, China, in 2000, 2004, and 2008, respectively.

He is currently an Assistant Professor with the School of Electrical Engineering, Xi'an Jiaotong University. His research interests include active power filters, power electronics inverters, reactive power compensation, and power quality control techniques.

• • •